

Finite element analysis applied to cornea reshaping

Delia Cabrera Fernández

University of Miami
Department of Ophthalmology
Miller School of Medicine
Bascom Palmer Eye Institute
Miami, Florida 33136
E-mail: dcabrera2@med.miami.edu

A. M. Niazy

The Aerospace Corporation
Los Angeles, California

R. M. Kurtz

University of California
Department of Ophthalmology
Irvine, California

G. P. Djotyan

KFKI-Research Institute for Particle and
Nuclear Physics
Budapest, Hungary

T. Juhasz

University of California
Department of Ophthalmology and Department of
Biomedical Engineering
Irvine, California

Abstract. A 2-D finite element model of the cornea is developed to simulate corneal reshaping and the resulting deformation induced by refractive surgery. In the numerical simulations, linear and nonlinear elastic models are applied when stiffness inhomogeneities varying with depth are considered. Multiple simulations are created that employ different geometric configurations for the removal of the corneal tissue. Side-by-side comparisons of the different constitutive laws are also performed. To facilitate the comparison, the material property constants are identified from the same experimental data, which are obtained from mechanical tests on corneal strips and membrane inflation experiments. We then validate the resulting models by comparing computed refractive power changes with clinical results. Tissue deformations created by simulated corneal tissue removal using finite elements are consistent with clinically observed postsurgical results. The model developed provides a much more predictable refractive outcome when the stiffness inhomogeneities of the cornea and nonlinearities of the deformations are included in the simulations. Finite element analysis is a useful tool for modeling surgical effects on the cornea and developing a better understanding of the biomechanics of the cornea. The creation of patient-specific simulations would allow surgical outcomes to be predicted based on individualized finite element models. © 2005 Society of Photo-Optical Instrumentation Engineers. [DOI: 10.1117/1.2136149]

Keywords: finite elements; corneal refractive surgery; biomechanics; tissue models; ultrafast laser technology; cornea.

Paper 04259R received Dec. 28, 2004; revised manuscript received Jun. 13, 2005; accepted for publication Jun. 23, 2005; published online Dec. 8, 2005. This paper is a revision of a paper presented at the SPIE conference on Ophthalmic Technologies XIV, Jan. 2004, San Jose, CA. The paper presented there appears (unrefereed) in SPIE proceedings Vol. 5314.

1 Introduction

In the past decade, refractive surgical techniques have met with considerable success and popularity, resulting in tremendous growth for the demand of visual corrections. As refractive procedures involving the cornea have proliferated, concerns over the long-term stability of these procedures have occupied a more prominent priority. Most techniques rely on altering the curvature of the cornea by removing corneal tissue, and the minimization of the postoperative refractive error has been a key clinical objective in all forms of refractive surgery. As the state of the art has advanced, so have the expectations for improved control over refractive outcomes. During the same period, more attention has been given to physiological and mechanical investigations of human and animal corneas, including investigations of the mechanical properties of the cornea. It is generally accepted that soft biological tissues are inhomogeneous, anisotropic, and nearly incompressible, viscoelastic materials.¹ The constitutive laws are nonlinear and time-history dependent.¹ This complicates

both experiments and the constitutive modeling needed to explain data.

The cornea performs two major functions: to protect the inner contents of the eye and to refract light. To do so, the cornea must maintain its strength and transparency. The main structural component of the cornea is the stroma, which provides most of the cornea's strength, and helps give the eye its shape. The refractive power of the cornea is determined by its index of refraction and by its radius of curvature, and accounts for over two-thirds of the optical power of the eye. The fact that 80% of the refractive power of the eye is determined by the cornea makes the alteration of the cornea the basis for most refractive procedures. The manipulation of the structural integrity of the cornea results in corneal shape changes, which then affect refractive properties of the cornea. Refractive procedures have been developed empirically with no detailed knowledge of intrinsic corneal behavior. While precise knowledge of shape is essential in modeling any mechanical system, including the cornea, it is clear that this cannot be the sole determinant of the results of refractive surgery.² Hence, an understanding of the biomechanical behavior of the cornea is

Address all correspondence to Delia Cabrera Fernández, Ophthalmology Dept., Bascom Palmer Eye Institute, Miller School of Medicine, University of Miami, 1638 NW 10th Ave., FL 33136. Tel: 305-326-6000. Fax: 305-326-6547. E-mail: dcabrera2@med.miami.edu

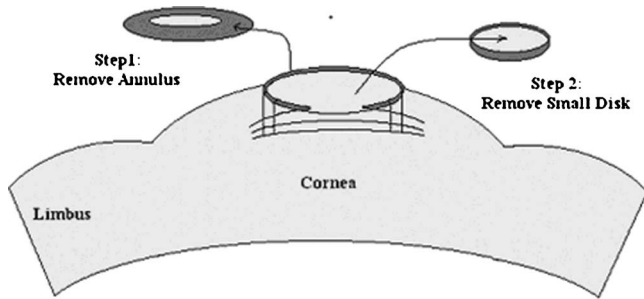


Fig. 1 A schematic view that shows the procedure followed to cut the corneal disks using the femtosecond laser.

vital for the development of predictive tools to aid the clinical management of patients.

Additionally, attempts to improve the postoperative visual outcome are not only limited by the precision of characterization techniques (i.e., topography, wavefront analysis, and refraction measurements), but also by the empirical surgical models that do not explicitly identify or account for significant sources of biomechanical response in the postoperative results. Consequently, there is a need for numerical simulations of corneal refractive surgery. With such simulations, we could investigate changes in corneal shape, taking into account the ablation profile and the biomechanical response, along with changes in mechanical properties of corneal tissue.

On the other hand, many soft tissues are homogeneous over certain regions. For instance, the corneoscleral connective tissue envelope of the eye can be considered homogeneous.³ However, the concept of homogeneity loses its meaning on a microscopic scale. So, zooming into the microscopic domain, inhomogeneity of the structure under consideration can no longer be ignored, which implies that bulk parameters, such as stresses and strains, are only valid concepts on the new scale but are no longer macroscopic. The sclera may also be considered homogeneous, but the cornea has different layers. Each layer is different in terms of the type and orientation of collagen fibrils, the interfibrillar matrix, and the cellular content.³ Therefore, the cornea should be considered as an inhomogeneous structure in a more rigorous model. The cornea may be thought of as a composite material having randomly oriented laminae embedded in a matrix with a very low shearing modulus.⁴ This greatly complicates the biomechanics of the cornea, and is one of the reasons for neglecting the inhomogeneities in the corneal structure in nearly all models developed so far. The basic idea is that assuming homogeneity is equivalent to an average of the existing microstructure. This kind of reasoning is common in soft tissue mechanics.⁵ Moreover, the determination of the appropriate constitutive assumptions is critical to mechanical models of surgical procedures. To the best of our knowledge, a finite element model of refractive surgery that introduces the inhomogeneities in the stiffness with depth variation has not been previously presented. Previous work has been limited to both the simulation of experimental conditions and interpretation of experimental results.^{1,6} Specifically, one heterogeneous model simulated the meridional transition in the stiffness between apex and limbus.⁶

In this work, we developed a finite element model that simulates the changes on corneal curvature after refractive surgery when stiffness inhomogeneities varying with depth are considered. This study also performed side-by-side comparisons of different constitutive laws that have been commonly used to model refractive surgery. To facilitate the comparison, the material property constants were identified from the same experimental data, which were obtained from mechanical tests on corneal strips⁷⁻⁹ and membrane inflation experiments.¹⁰ The resulting model was also validated by comparing computed refractive power changes with clinical results.

2 Methods

2.1 Mechanical Measurement of the Elasticity Parameters

To measure directly the elastic modulus of a small sample, a deformation to a known force is usually measured. A mechanical technique was used to measure elasticity distributions in large tissue samples.⁷⁻⁹ This technique produces nearly direct measures of elasticity and is widely accepted.¹¹⁻¹⁴ The entire thickness of an *ex-vivo* human cornea was used ($857\ \mu\text{m}$) in the experimental protocol developed.⁷⁻⁹ The *ex-vivo* human cornea was obtained from a human donor 70 years old. The specimen was stored in corneal storage medium (Optisol, Chiron, Irvine, California) within 3 h after patient death and was tested within 2 days. A femtosecond surgical laser,^{15,16} capable of cutting the tissue with high accuracy, was used to make five cuts at increasing corneal depths. Thus, a series of five circular disks or layers approximately 140 to $350\ \mu\text{m}$ thick and $5\ \text{mm}$ in diameter were obtained (see Fig. 1).

We note that to produce disks for mechanical measurements, a plane was cut parallel to the applanated anterior corneal surface. If these disks assume natural curvatures in the intact globe, resulting anterior and posterior surfaces would no longer be planar when the applanating contact lens is removed after resection. In practice, an unloaded tissue block has insufficient rigidity to revert to its loaded curvature and assumes a planar shape through surface tension when placed on a flat surface.¹ The resulting disk sections have uniform thickness with parallel, planar surfaces.¹⁷ Each sample was positioned horizontally on the rigid platform of a scale (0.01-g resolution). Deformations were applied with an 8-mm -diam piston covering the entire surface of the sample. The piston was lowered onto the sample using a dc stepper motor driven positioning system (Unislid MB2506p5j-s2.5, Velmex Incorporated, East Bloomfield, New York). The piston was then slowly pulled back until a force of 0.01 Newton was reached. At fixed time intervals, the piston was lowered a single step and five consecutive force measurements were performed for each corneal button.⁷ After each trial, there was a waiting period to allow the sample to relax. For the next trial, the 0.01 Newton preload point is found as described earlier, and the measurement was repeated. Consecutive measurements were used to ensure that deformations were applied at a rate slow enough to measure the static elastic properties of the sample. Details about the reproducibility and error analysis of the mechanical measurements using this technique have been reported previously by Erkamp et al.⁷

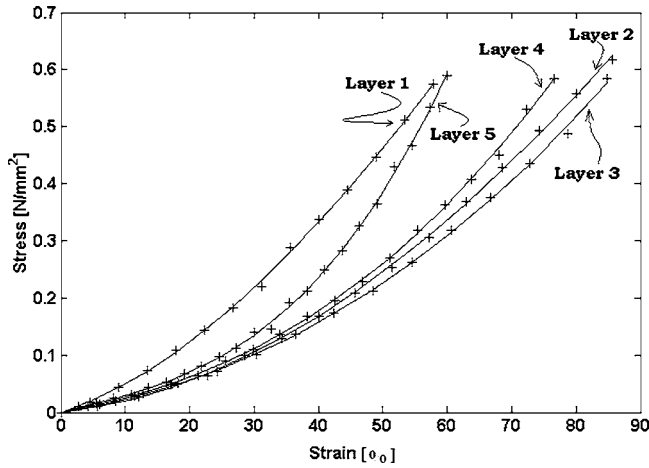


Fig. 2 Stress-strain curves for each layer, and for 10% of deformation. A third-order polynomial was fitted to the raw data obtained experimentally. The solid lines are for the fitted curves, and the crosses are for the raw data.

The deformation measurements were then converted to an elastic modulus, where the conversion uses prior calibration of the system with plastisol samples of known Young's modulus.⁷ A third-order polynomial was fitted to the raw data obtained experimentally. The stress-strain data for each layer and for 10% of deformation is shown in Fig. 2. Layer 1 is the outermost layer. Since the width of the strip is sufficiently narrow ($t/R < 0.1$, assuming a radius of curvature of 7.8 mm for the intact eye), the possibility for changes in the transverse direction associated to the bending effect can be neglected.¹⁴ Moreover, because the corneal disk is thin when compared to its length, the bending stress profile should have little effect on the average stress through the corneal layer. Note that our reported values of stress and strain should, therefore, be interpreted as averages through the corneal strip. The measured Young's elastic modulus as a function of tissue depth is shown in Fig. 3. Elasticity variations with depth are shown for 10, 20, and 30% deformations.

2.2 Computer Simulations

The general aspheric shape (steeper centrally and flatter peripherally) of the cornea and the variation in the thickness is considered in all the simulations developed. Figure 4(a) shows the details of the geometric configuration used in the finite element model. The cornea was assumed to have a radius of 7.56 mm and a base diameter of 11.5 mm.¹⁸ Corneal thickness is assumed to vary linearly along the meridional direction [i.e., from P_C to P_L , see Fig. 4(a)]. It is taken to be 0.5 mm at the center (T_C) and 0.67 mm at the limbus (T_L). The total area covered by the half of the corneal model was 3.6 mm². The central corneal thickness (T_C) is measured along the anterior-posterior axis of the eye that actually represents the axis of symmetry. The direction along this axis is used to measure any change in apical or central thickness. The radius is drawn from the geometric center of the corneal anterior center. The corneal thickness was divided in five layers to simulate the variation in stiffness through the thickness [see Fig. 4(a)]. Furthermore, the cornea is also modeled as an axisymmetric structure, with the axis of symmetry along the

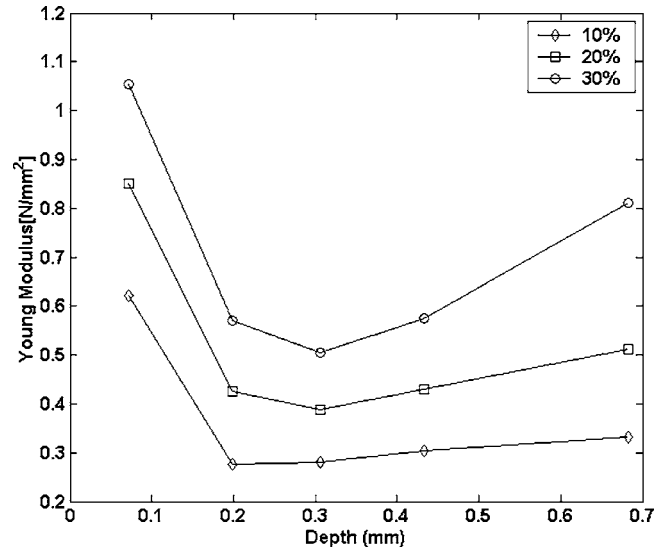


Fig. 3 Elasticity variations with depth are shown for 10, 20, and 30% deformations. Depth is measured at the midpoint of the corneal disk.

anterior-posterior axis of the eye (see Fig. 4). This greatly reduces the complexity of the analysis of the 3-D structure to a single, 2-D finite element analysis.

Since the change in curvature between the cornea and sclera suggests circumferential fibrils from the mechanical point of view, the boundary nodes at the edge of the cornea through the thickness were assumed to be fixed in displacement and free to rotate about the axis tangent to the boundary circle [see Fig. 4(b)]. Also, due to the assumption of axis symmetry, displacements at the nodes through the apex were fixed in the horizontal direction (x axis) and free in the vertical direction (y axis) [see Fig. 4(b)]. Any role played by the sclera was ignored.

Also note that *in vivo*, the cornea is continuously subjected to the intraocular pressure and deforms in response to the surgical treatment. Thus, to simulate the effects of the refractive surgery only, two benchmark models were constructed: 1. intact cornea baseline [see Fig. 4(b)], and 2. removed lenticle-changed cornea [see Fig. 4(c)]. Both models were subjected to the same intraocular pressure. Differences in the predicted deformation of these two models being the result of the refractive surgery procedure could be used to calculate a change in corneal curvature. On the other hand, three different lenses were used for simulating the surgery and testing the models: 1. a convex-convex lenticle with a central corneal thickness of 100 μm and a diameter of 4 mm [see Fig. 4(c)]; 2. a convex-convex lenticle with a central corneal thickness of 120 μm and a diameter of 4 mm, and 3. a plano-convex lenticle with a central corneal thickness of 100 μm and a diameter of 4 mm [see Fig. 4(c), inset picture at right]. To simulate the intrastromal cavity arising in the place of the removed lenticle, we used gap elements.¹⁹⁻²¹ The gap is intended to model point-to-point contact and is applied to surfaces that may come into contact [see Fig. 4(c)]. The surfaces that will be in contact could be defined as stiff surfaces that these gap elements cannot penetrate, as the gap is incrementally closed. The collapse of the intrastromal cavity is equivalent to removing a thin lens of the same shape as the cavity.²² It is assumed

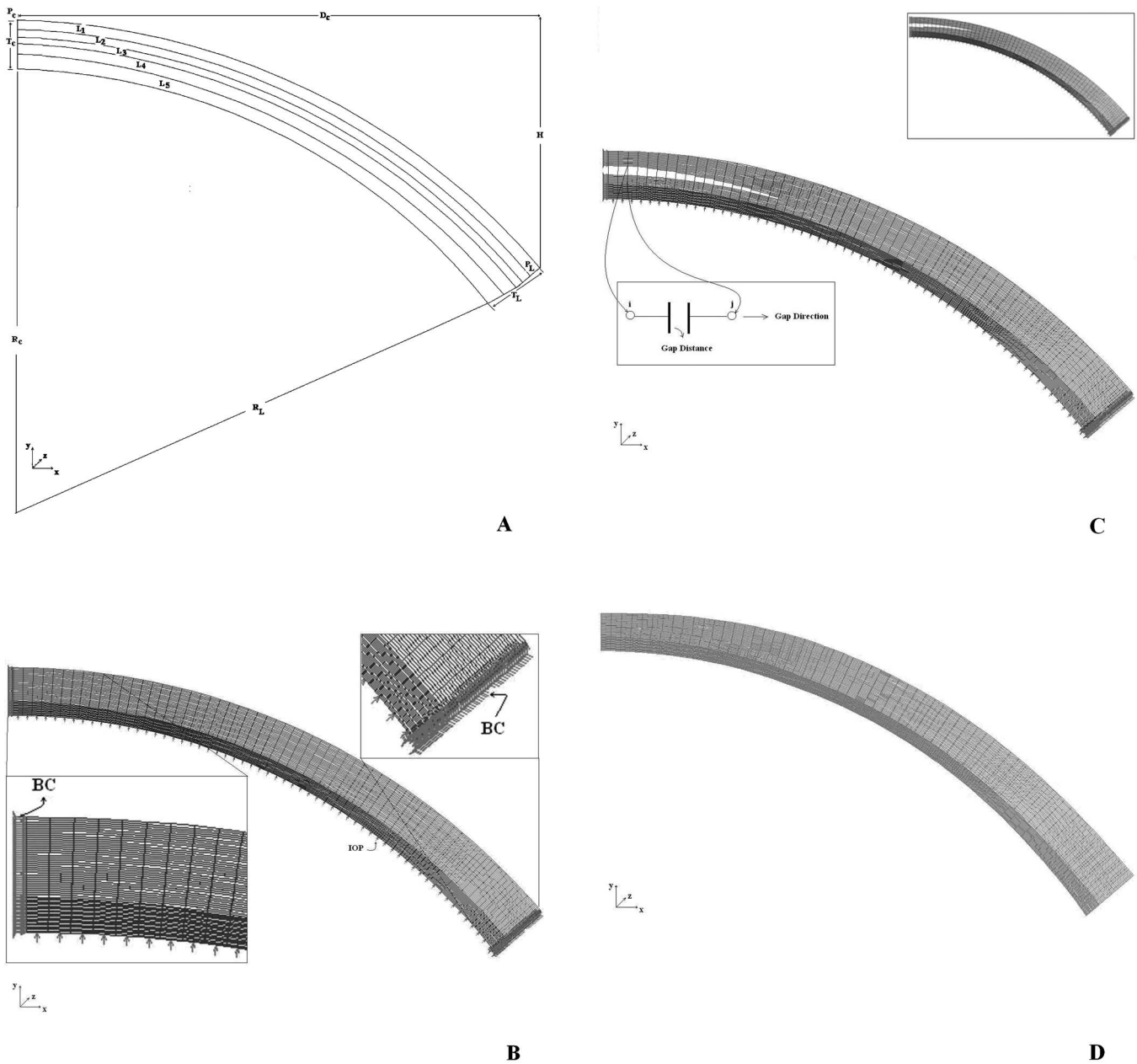


Fig. 4 Illustration is used in deriving the finite element analysis. (a) Geometric diagram of half of a corneal section. Note that T_C is the apical corneal thickness (0.5 mm). T_L is the peripheral corneal thickness (0.67 mm) at a location P_L a distance D_C (6 mm) from the corneal apex. The corneal segment is divided into five layers (L_1 to L_5). R_C is the apical radius (7.56 mm) of the anterior corneal surface at the point P_C . R_L is the radius of the anterior corneal surface at the point P_L (i.e., at the limbus). H is the height of the cornea (2.5 mm) measured from a plane at the point P_L . (b) Finite element model for the intact cornea-baseline model. Note that the anterior and posterior surfaces follow concentric circular arcs defined by the standard size of the cornea. Also, the boundary conditions (arrows) are shown at the geometric axis and at the edge of the cornea (i.e., at the limbus) along with the intraocular pressure (IOP) on the posterior surface. (c) Finite element model for the removed lenticle-changed cornea model. A convex-convex lenticle simulates the removal of corneal tissue. Note that the anterior corneal segment is thicker at the edges than at the center, having a central thickness of $160 \mu\text{m}$. The convex-convex lens has a diameter of 4 mm and a central thickness of $100 \mu\text{m}$. The area covered by the lenticle is 0.13 mm^2 in the 2-D cross section. The inset picture in the upper-right part shows the removed lenticle-changed cornea model for a plano-convex lenticle. Note that the anterior corneal segment has a uniform thickness of $160 \mu\text{m}$. The plano-convex lenticle has a diameter of 4 mm and a central thickness of $100 \mu\text{m}$. The inset picture in the left-lower part shows the details for the two-node gap elements. Note that each gap element is defined by two nodes: i and j . The direction of the gap in the undeformed state is defined as the line connecting node i to node j . The gap distance is the maximum allowable relative displacement between the two nodes along the gap direction. (d) Finite element model for the removed lenticle-changed cornea model after the removal of a convex-convex lenticle.

that the cavity collapses completely without any gaps and with only the stretching or compression of the elements required to achieve collapse.

The anterior corneal segment, being thicker at the edges than at the center, was simulated with a central corneal thickness of 160 μm . Figure 4(d) shows the geometry of the model after the collapse of the cavity (i.e., after the removal of the convex-convex lenticle). The cornea was loaded by a uniform pressure distribution, which was taken to be 0.002 N/mm². This pressure is equivalent to a mercury column of 15-mm height.²³ The intraocular pressure was applied normal to the posterior surface of the model [see Fig. 2(b)]. The loading produced by the eyelids and the extraocular muscles was ignored. Corneal tissue was assumed to behave as a nearly incompressible material with a Poisson's ratio equal to 0.49. Furthermore, four-node isoparametric axisymmetric 2-D elements were used in the simulations, thus only two translational degrees of freedom were considered for each node. To generate the mesh, several mesh densities were tested to ensure accurate and consistent convergence. Mesh that covered half of the cornea consisted of 3600 elements and 3721 nodes; when 60 elements were used across the thickness, and about 60 elements were implemented along the meridian, it resulted in a total of 7442 equations. More elements were attributed to the anterior corneal layers for higher accuracy of the modeling.

A commercially available finite element analysis program (COSMOS/M, Structural Research and Analysis Corporation, Santa Monica, California) was used for the implementation of the numerical simulations. A Newton-Raphson procedure, an iterative solution method with high quadratic convergence rate, was used in the nonlinear analysis.¹⁹⁻²¹ In this procedure, the tangential stiffness matrix is formed and decomposed at each iteration within a particular solution step. A force control technique is used to control the progress of the computations along the equilibrium paths of the system.¹⁹⁻²¹ In this technique, applied loads are used as the prescribed variables, and the loads are incrementally applied using time curves. Convergence was reached in about 7 or 8 iterations for a total of about 100 solutions steps. The relative displacement tolerance for equilibrium iterations was 0.001 mm.

To facilitate the comparison of different constitutive laws, four different models were constructed:

2.2.1 *Inhomogeneous and nonlinear elastic isotropy model*

The finite element model was based on an inhomogeneous and nonlinearly elastic, isotropic formulation. Material nonlinearity was modeled with a nonlinear stress-strain relationship obtained from direct mechanical measurements for 10% of deformation (see Fig. 2).

2.2.2 *Homogeneous and nonlinear elastic isotropy model*

The finite element model was based on a homogeneous and nonlinearly elastic, isotropic formulation. Material nonlinearity properties were based on the average values identified from the membrane inflation tests.¹⁰ Material nonlinearity was modeled with a nonlinear stress-strain relationship given by:

Table 1 Values of Young's elastic modulus for 10% deformations.

Layers	Young's elastic modulus (N/mm ²)
L1	0.622
L2	0.275
L3	0.279
L4	0.304
L5	0.331
Average	0.363

$$\sigma = \alpha[\exp(\beta \cdot \varepsilon) - 1], \quad (1)$$

where σ is the stress and ε is the strain. The material constants α and β are equal to 17.5×10^{-4} N/mm² and 48.3, respectively.¹⁰

2.2.3 *Inhomogeneous and linear elastic isotropy model*

The finite element model was constructed following a linear elastic isotropy formulation, but considering a different Young's elastic modulus for each layer. Table 1 shows explicitly the values measured for each layer that were also shown in Fig. 3.

2.2.4 *Homogeneous and linear elastic isotropy model*

The biomechanical model was constructed following a linear elastic isotropy formulation, but considering the same Young's elastic modulus for each layer. The value used was the average Young's elastic modulus (0.363 N/mm²) calculated using the specific value at each layer (see Table 1).

Curvature changes were calculated along the meridional direction on the anterior surface of the cornea. A cubic spline function was fitted to all of the nodes along the corneal anterior surface.²⁴ Since the spline fitting process calculates the normal direction at each point on the curve, then the radius of curvature at each point is determined from the length of the line that extends normal to the corneal anterior surface from the point to the geometric axis of the cornea [see Fig. 4(a)]. The average radii of curvatures were then computed from data values within a 3-mm-diameter zone at the corneal apex. The corneal power in diopters was computed by dividing 0.376 (representing the difference between the refractive indices of the air and the cornea) by the corneal radius of curvature in meters.

Finally, a side-by-side comparison was developed using the four models defined before. The comparison is particularly important to determine the effect of stiffness variations through the thickness on the shape of the human cornea, and its consequences on the predictability of the refractive surgery models.

2.3 *Clinical Data*

In this section, we briefly describe the clinical results that were simulated using the previous models. These results were

Table 2 Results obtained using different constitutive laws for a convex-convex lenticle with a central thickness of 100 μm and a diameter of 4 mm.

Model	Average curvature change in a 3-mm zone diameter (diopters)	Change in central corneal thickness (μm)
Inhomogeneous and nonlinear elastic isotropy	-12.56	-98.60
Homogeneous and nonlinear elastic isotropy	-14.05	-96.70
Inhomogeneous and linear elastic isotropy	-24.62	-96.90
Homogeneous and linear elastic isotropy	-22.88	-97.30

taken from a previously published report.²⁵ Specifically, we compare the outcome of the simulations with clinical results after picosecond laser keratomileusis (PLK).

2.3.1 Picosecond laser keratomileusis

Clinical results from a total of eight nonsighted eyes treated with tapered lenticle (convex-convex lens), myopic PLK were considered in the simulations developed. All procedures were performed using the ISL 4000 Nd:YLF picosecond laser (Intelligent Surgical Lasers, San Diego, California), which creates the anterior and posterior lenticular surfaces with a computer-controlled laser beam focused intrastromally.²⁵ A lenticle diameter of 4 mm and two different lenticle thicknesses (100, 120 μm) were used. The flap thickness was approximately 160 μm in each case, as estimated postoperatively from ultrasonic biomicroscopy.²⁵ Results were grouped into two treatment categories: group 1 (4 mm/100- μm lenticle, $N=2$) and group 2 (4 mm/120- μm lenticle, $N=6$). Changes in corneal curvature and central corneal thickness were assessed postoperatively at intervals of 1 week and at 1, 3, and 6 months.^{25,26} A more detailed description about the surgical technique and clinical results has been reported by Bryant and Juhasz.²⁵

3 Results

3.1 Side-by-Side Comparison between the Models

A comparison of the capabilities of the different models described before was developed. The objective was to determine the average corneal curvature change in a 3-mm zone, and the alter in central corneal thickness based on the material properties used from both the membrane inflation experiments¹⁰ and the direct mechanical measurements.⁷⁻⁹ Table 2 shows the results obtained for the models that considered a convex-convex lenticle with a central corneal thickness of 100 μm and a diameter of 4 mm. The results for the models considering a convex-convex lenticle with a central corneal thickness of 120 μm and a diameter of 4 mm are shown in Table 3.

As can be seen from the results shown in the tables, the smallest average curvature change in a 3-mm zone diameter was obtained when stiffness variations with depth were considered, along with material properties nonlinearities. Furthermore, the biggest change in central corneal thickness was also obtained in this case.

Table 3 Results obtained using different constitutive laws for a convex-convex lenticle with a central thickness of 120 μm and a diameter of 4 mm.

Model	Average curvature change in a 3-mm zone diameter (diopters)	Change in central corneal thickness (μm)
Inhomogeneous and nonlinear elastic isotropy	-14.68	-118.50
Homogeneous and nonlinear elastic isotropy	-16.51	-116.30
Inhomogeneous and linear elastic isotropy	-25.59	-116.80
Homogeneous and linear elastic isotropy	-24.53	-117.41

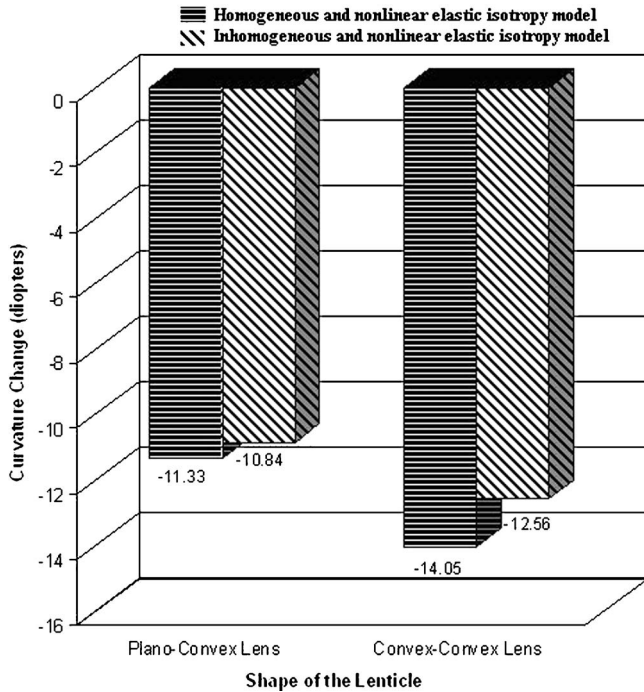


Fig. 5 Effect of the shape of the lenticle on corneal curvature. The horizontal line bars stand for the homogeneous and nonlinear elastic isotropy's model, and the diagonal line bars represent the curvature changes for the inhomogeneous and nonlinear elastic isotropy's model.

3.2 Effect of the Shape of the Lenticle

The effect of the lenticle's shape on curvature and central flattening of the cornea was also studied when stiffness variations with depth were considered, along with material properties nonlinearities. For comparison, a convex-convex lens shape [see Fig. 4(c)] and a plano-convex lenticle shape [see Fig. 4(c), inset picture in the upper-right part] were used in the modeling, both with the same central corneal thickness (100 μm), same diameter (4 mm), and with approximately the same area (about 0.13 mm²). The total area covered by half of the corneal model was 3.6 mm². The volume of the removed tissue was assumed the same in both models. Note that the cornea with the two different configurations for the lenticle pattern also has different configurations of its anterior segment. A plano-convex lenticle model has a uniform thickness for its anterior segment [see Fig. 4(c), inset picture in the upper-right part], and the convex-convex model has its anterior segment thicker at the edges than at the center [Fig. 4(c)]. Moreover, both cornea's models have an anterior segment thickness that is in its central axis (i.e., at the apex) equal to 160 μm.

The model with a convex-convex lenticle (nonuniform anterior corneal segment thickness) leaves a stromal bed behind, which is thicker centrally than peripherally, giving a bigger correction within the central zone [see Figs. 4(c) and 5]. The convex-convex lenticle created more central flattening of the cornea than the plano-convex lens when stiffness variations with depth were introduced.

It is interesting to note how close the changes in curvature are for both models (homogeneous and inhomogeneous) when

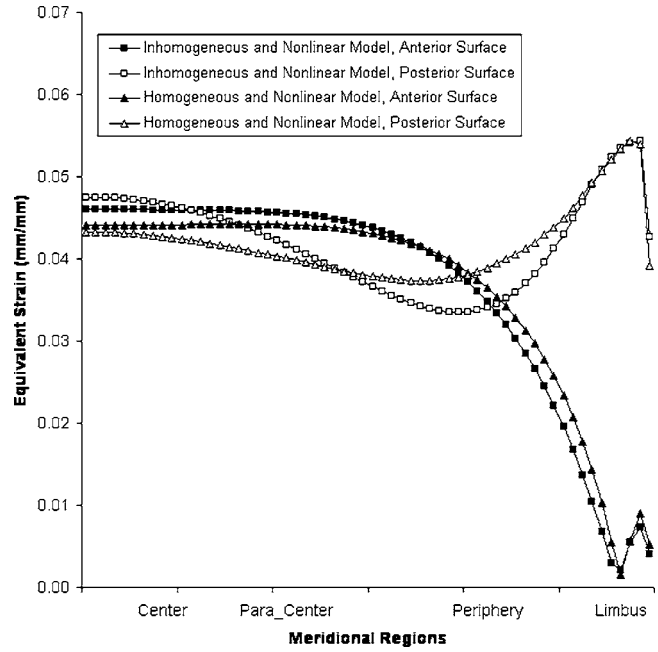


Fig. 6 The pressure-induced meridional strains at the anterior and posterior corneal surfaces.

a plano-convex lenticle is used. This type of lenticle leads to the stroma being cut parallel to the anterior corneal surface, resulting in no cut ends of the fibrils to reconnect.²⁷ It seems a reasonable proposition that the cut of the layers in a more distorting manner using a convex-convex lenticle offers probably a singular advantage with respect to the distribution of the cohesive strengths between the anterior and posterior corneal layers. This might also afford better opportunities for future experiments to determine how to optimize the corneal structural changes as a function of the lack of uniformity in its underlying structure to make the refractive correction more reliable.

3.3 Corneal Strain Analysis

In this section, meridional and depth-dependent strains predicted by the finite element model are analyzed. Only the baseline models are used for the comparison (i.e., only response to pressure loading is considered). Figure 6 shows the meridional variations of the equivalent strain for the inhomogeneous and nonlinear model, and the homogeneous and nonlinear model, respectively. Four regions of the cornea were defined: 1. central region (covering the central 3-mm zone), 2. para-central region (1.5 to 3.5 mm from the corneal apex), 3. peripheral region (3.5 to 5.5 mm from the corneal apex), and 4. limbal region (5.5 to 6 mm from the corneal apex).

The equivalent strain is calculated from:²⁷

$$\text{equivalent strain} = 2 \left[\left(\frac{\epsilon_1 + \epsilon_2}{3} \right)^{1/2} \right], \quad (2)$$

where

$$\epsilon_1 = \frac{1}{2} [(\epsilon_x - \epsilon^*)^2 + (\epsilon_y - \epsilon^*)^2 + (\epsilon_z - \epsilon^*)^2], \quad (3)$$

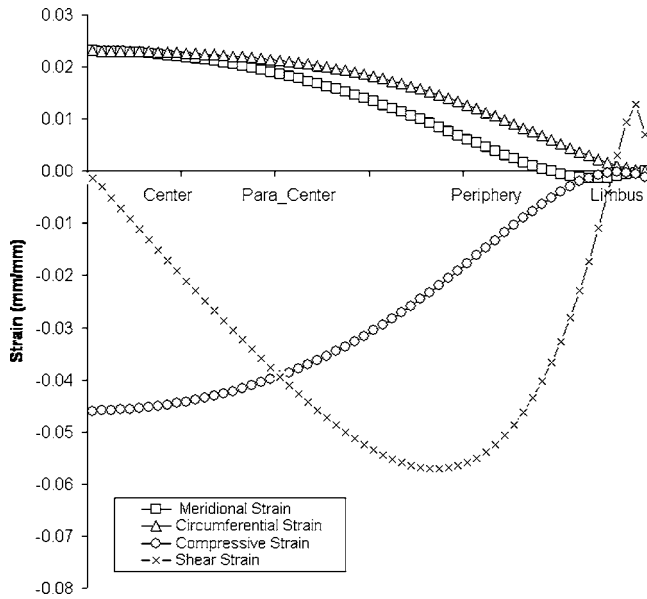


Fig. 7 Meridional, compressive, circumferential, and shear strains at the anterior corneal surface for the inhomogeneous and nonlinear model.

$$\varepsilon_2 = \frac{[(\Sigma_{xy})^2 + (\Sigma_{xz})^2 + (\Sigma_{yz})^2]}{4}, \quad (4)$$

denoting the shear strain, and

$$\varepsilon^* = \frac{(\varepsilon_x + \varepsilon_y + \varepsilon_z)}{3}. \quad (5)$$

Note that the anterior-side strains were smaller than the corresponding posterior-side strains at the central meridional region for the inhomogeneous and nonlinear model. This trend is reversed for the homogeneous and nonlinear model. The largest difference between the anterior and posterior-side strains was seen at the limbal region. Furthermore, the posterior-side strains were smaller at the periphery for the inhomogeneous and nonlinear model. The graph also reveals that the para-central and peripheral parts of the posterior corneal surface deformed less in response to pressure loading compared to the central cornea and the limbus. The deformations in response to pressure loading predicted by the inhomogeneous and nonlinear model are in agreement with the experimentally documented regional differences found by Hjortdal.¹ Whether the measured uniformity in the anterior-side strain is related to the more parallel-ordered fibril organization of the central and para-central regions, compared with the periphery and limbus, remains to be investigated.²⁸ As a matter of fact, it is this uneven arrangement of the fibers that makes constructing an adequate finite element model of the cornea so difficult.

The meridional, compressive, circumferential, and shear strains at the anterior and posterior corneal surface for the inhomogeneous and nonlinear model are shown in Figs. 7 and 8. The para-central and peripheral regions deformed less in the meridional direction compared with the circumferential direction, suggesting a meridional strength of these parts.

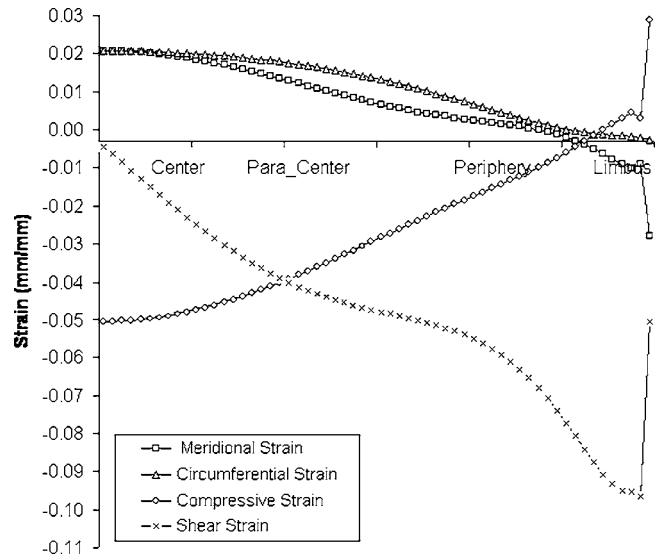


Fig. 8 Meridional, compressive, circumferential, and shear strains at the posterior corneal surface for the inhomogeneous and nonlinear model.

Previous work has reported that the strain distribution on the anterior surface is highly nonuniform.⁶ Moreover, interferometric measurements of the corneal deformations at physiological pressures indicate that a dip occurs at a radial distance of 3 to 4 mm from the apex.²⁹ This high nonuniformity in strain was not predicted by the models tested, even when the inhomogeneities in stiffness through the thickness were considered. Instead, the models predicted a meridional strain, which decreased from a maximum at the apex. Since only the corneal mechanical properties were directly measured and no information was obtained on the mechanical properties of the sclera, this led us to hypothesize that this could be one of the reasons for the mismatch.

3.4 Computer Simulation and Clinical Data

Computer simulations were compared with the clinical results 1 month after picosecond laser keratomileusis procedures.²⁵ These clinical results were simulated using both the homogeneous and inhomogeneous nonlinear isotropy models presented before. Table 4 reproduces the achieved corrections obtained at 1 month for two of the three treatment categories defined by Bryant and Juhasz.²⁵ The same input parameters defined by Bryant and Juhasz were used in our finite element models. The predictions provided by the inhomogeneous and nonlinear elastic isotropy model are also shown for comparison purposes (see Table 4). The changes in curvature were averaged in a 3-mm zone diameter.

The model considering the inhomogeneities in stiffness overpredicted the curvature's changes by a smaller margin when compared to the model that only took into account the material nonlinearities. The overprediction given by the inhomogeneous model was approximately -1.26 diopters for the 4 mm/100 μm lenticle, and -1.58 diopters for the 4 mm/120 μm lenticle. The average flattening overprediction was equal to -1.42 diopters. Moreover, the inhomogeneous model also overestimated the thickness changes by

Table 4 Comparison between the predictions for myopic corrections provided by the finite element models, and the clinical data outcomes of PLK surgical procedures at 1 month.

Lenticle's parameters	Clinical results		Inhomogeneous and nonlinear elastic isotropy model		Homogeneous and nonlinear elastic isotropy model	
	ΔK (diopters)	ΔT (μm)	ΔK (diopters)	ΔT (μm)	ΔK (diopters)	ΔT (μm)
Group 1 (4 mm/100 μm)	-11.3 ± 0.0	-84 ± 8	-12.56	98.60	-14.05	-96
Group 2 (4 mm/120 μm)	-13.1 ± 2.7	-98 ± 11	-14.68	118.5	-16.51	-117

13.4 μm for the 4 mm/100 μm lenticle and 19.2 μm for the 4 mm/120 μm lenticle. The average thinning overprediction was equal to 16.3 μm .

As can be seen, both the flattening and thinning overpredictions were reduced when the stiffness inhomogeneities were included in the finite element formulation. The predictions of the nonlinear-homogeneous and nonlinear-inhomogeneous models versus the achieved curvature changes at 1 month, and for the two clinical groups, are shown in Fig. 9. Data points represent the values for each group of patients. Error bars represent standard deviations of the measured curvature changes.

3.5 Sensitivity Analysis

A sensitivity study was performed for the inhomogeneous and nonlinear isotropy model. A design variable was perturbed at a time by a specified value, while the rest of the design variables were kept unchanged. The perturbed design variables were defined either by the actual values or by a perturbation ratio with respect to the initial value. To determine the sensi-

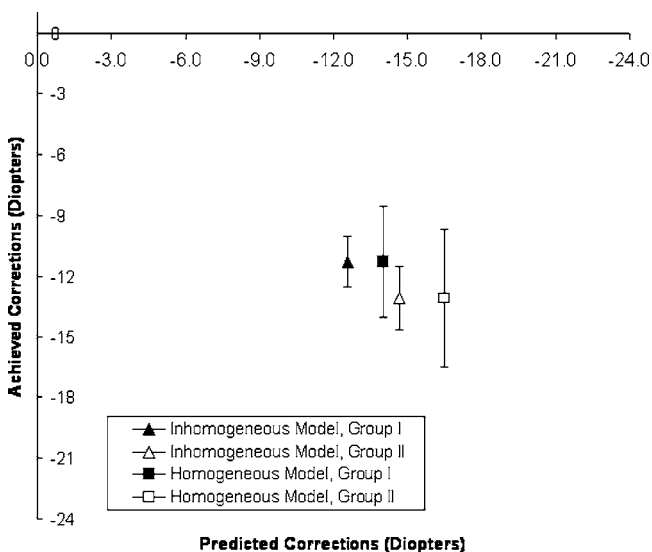


Fig. 9 Curvature changes at 1 month for each patient versus changes in curvature predicted by the finite element models in a 3-mm diameter zone.

tivity of the model, it was necessary to establish a baseline model. This model was derived from one of the treatment groups (group 1) defined in Table 4. The effect on corneal curvature of the intraocular pressure, central corneal thickness, and Poisson ratio was investigated. Table 5 shows the range of the parameters used in the sensitivity analysis.

Figure 10 shows the results when the intraocular pressure, central corneal thickness, and Poisson ratio were varied. Note that the central corneal curvature change is not significant in the normal physiological range (15 to 20 mmHg). The central curvature changed by as much as 10% below this range [see Fig. 10(a)]. The effect of corneal thickness variation on predicted curvature changes is shown in Fig. 10(b) and, as expected, thin corneas flatten more. The central curvature change distorted by as much as 20% in this range. In a thinner cornea, less uncut tissue is left behind once the lenticle is removed; whereas in a thicker cornea, more uncut tissue is left behind, which is less easily displaced and therefore produces less central flattening. Moreover, the effect of Poisson ratio variation on the predicted curvature changes is shown in Fig. 10(c). Note that the refractive change is not significant.

Furthermore, to evaluate the sensitivity of the predicted curvature changes to the material properties, the group 1 (4 mm/100 μm) results were recomputed considering a modulus of elasticity reduction of about 15% from the initial values used for all the layers. Thus, the finite element model was softer than the baseline model. The predicted curvature change of the group 1 procedure was -15.32 diopters, compared with the baseline model result of -12.56 diopters.

4 Discussion and Conclusions

Mechanical studies of the cornea are important for modeling the immediate behavior of the surgically altered cornea, be-

Table 5 Parameters used in the sensitivity analysis.

Parameters	Range
Intraocular pressure	10, 15, 20, 25, 30, 35 mm Hg
Central corneal thickness	490, 495, 500, 505, 510 μm
Poisson ratio	0.3, 0.39, 0.49

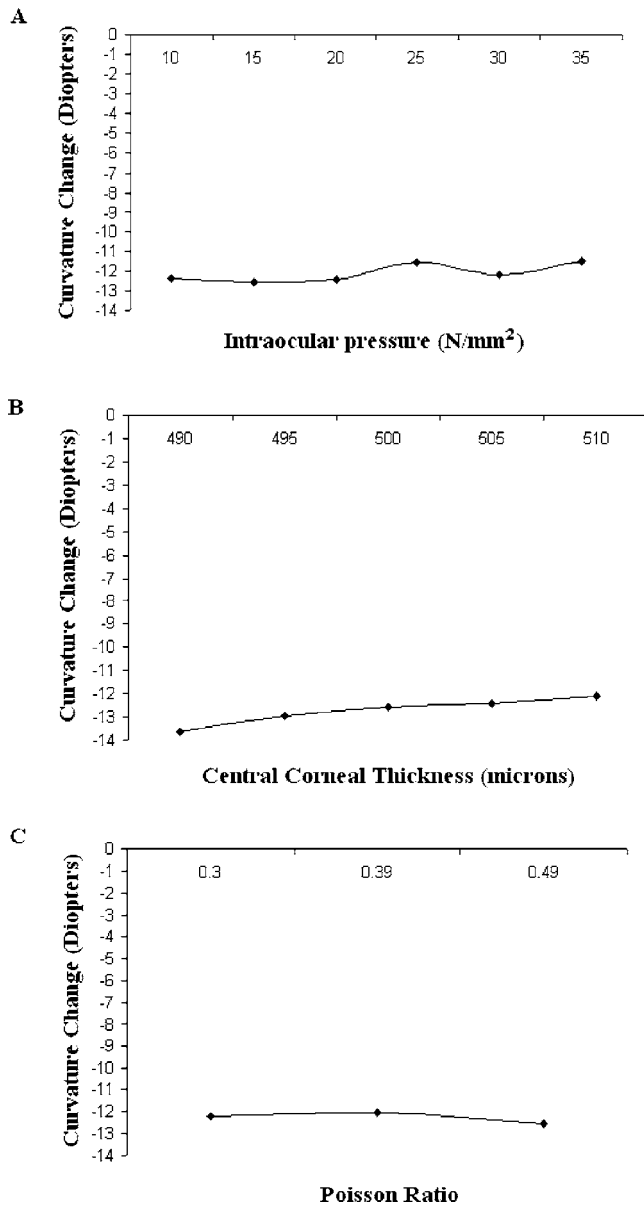


Fig. 10 Sensitivity analysis results obtained when the intraocular pressure, central corneal thickness, and Poisson ratio were varied.

sides increasing our knowledge about corneal biophysics. Most biological tissue is inhomogeneous; however, biological tissue may be homogeneous in certain areas. For example, the scleral coat of the eye is relatively homogeneous but the cornea is not. The cornea is really a composite layered material made up of collagen fibrils and ground substance. Each of these distinct layers (Bowman, anterior and posterior stroma, and Descemet), is homogeneous in its own venue, but taken together are not. This of course complicates the study of corneal biomechanics, because all of the methods employed to model structures assume homogeneity of that structure to produce meaningful results. Thus, some average microstructure is in general assumed. On the other hand, measurement of gross material properties in substances such as the cornea, with significant internal structure, results in some error. To predict the corneal response after surgery, we developed and tested an

inhomogeneous and nonlinear elastic isotropy model. From our experimental and numerical studies, it appears that inclusion of stiffness inhomogeneities varying with depth is essential to obtain accurate predictive capabilities. We have shown that the predictability of the surgical outcome is improved when the inhomogeneities of the cornea and nonlinearities of the deformations are included in the finite element simulations. Thus, we believe that the inhomogeneous model is a more accurate representation of the corneal material properties to model the biomechanical effects of refractive surgery. However, we would like to point out that we cannot generalize yet from the results of modeling, since only one *ex-vivo* human cornea has been used to obtain the elasticity properties varying with depth.

Furthermore, the fact that the materially nonlinear law works well for membrane inflation and direct mechanical experiments does not necessarily imply that it will work well for refractive surgery.^{6,10} In the specific case where elasticity data were obtained from membrane inflation experiments, the material properties used for modeling the surgery were obtained from intact corneas of ages between 20 to 69.¹⁰ Moreover, the corneal stroma becomes stiffer with age, thus the failure to average age variations significantly degrades the validation of the model on an individual basis. On the other hand, the elasticity data obtained from the direct mechanical measurements were obtained only from one *ex-vivo* human cornea; thus, the validation of the model for a large population is also a question that needs to be better explored by extending the direct mechanical measurements to a large number of tissue samples. Moreover, in a complex nonhomogeneous layered material, such as the cornea, the act of cutting the cornea into strips can introduce errors in measurement. Since a swollen cornea is stiffer, some underestimation of the elastic modulus is also expected, which can affect the results when compared to normal unswollen cornea. Consequently, our modeling results could be affected by all of the previous facts.

The simulations also revealed that the para-central and peripheral parts of the cornea deformed less in response to pressure loading compared to the central cornea and the limbus. Furthermore, the deformations in response to pressure loading predicted by the nonhomogeneous and nonlinear model showed that the para-central region is mechanically enhanced in the meridional direction. This result is in agreement with the experimentally documented regional differences found by Hjortdal.¹

On the other hand, the sensitivity analysis performed for the inhomogeneous and nonlinear isotropy model showed the influence on the predicted refractive data when the intraocular pressure, central corneal thickness, material properties, and Poisson ratio were perturbed. However, we note that an accurate estimation of the distributions of each input is required to meaningfully estimate the standard deviation of the finite element solution. For example, boundary conditions are very important in the finite element modeling of the human cornea. The deformation at the limbus area especially needs to be investigated. However, no mechanical properties are known for the limbus. Other important sources of potential error in the finite element model include its inability to account for wound healing effects, hydration changes, and its lack of anisotropy. Although some problems remain to be solved, the only consistent measure of the accuracy of a finite element

model of the human cornea is a direct comparison of the model's predictions with actual clinical results, as was performed here.

To refine our predictions, further inputs from additional experiments considering a larger number of *ex-vivo* human cornea will be necessary.^{30,31} These additional experiments should provide information about the material properties along the meridional direction (including the scleral region). Taken all together with the measured stiffness, inhomogeneities could provide the basis of a refined finite element model.

Our finite element model gives results that are in agreement with experimental and clinical observations. However, the model must be validated and fine tuned based on a retrospective study on individual eyes for a statistically significant set of data, before a prospective clinical trial is warranted using the finite element formulation. In addition, the model can be fine tuned by means of more complete information using accurate estimates of the distribution of each input. Our ultimate goal is to gain a better understanding of the cornea's biomechanical response to standardized ablation profiles.

Acknowledgments

This research was funded by NIH 1 R01 EY014163-01 and NIH R44 EY 12340-02. The authors are grateful to Stanislav Emelianov of the Biomedical Ultrasound Laboratory, and to Gregory J. Spooner from the Center of Ultrafast Optics and Science for their major contributions to the corneal strips measurement experiments and for providing the mechanical properties data we used in this research.

References

1. J. O. Hjortdal, "Regional elastic performance of the human cornea," *J. Biomech.* **29**(7), 931–942 (1996).
2. J. J. Rowsey and H. D. Balye, "Prospective evaluation of radial keratotomy," *Ophthalmology* **95**, 322–334 (1988).
3. K. M. Meek and G. F. Elliot, "The organization of collagen fibrils in the human corneal stroma: a synchrotron x-ray diffraction study," *Curr. Eye Res.* **2**, 471–477 (1987).
4. T. Huang and T. Bisarasin, "Corneal curvature change due to structural alteration by Radial Keratotomy," *ASME J. Biomech. Eng.* **110**, 249–253 (1988).
5. Y. C. Fung, *Biomechanics: Mechanical Properties of Living Tissues*, pp. 211, Springer-Verlag, New York (1981).
6. T. J. Shin and R. P. Vito, "The distribution of strain in the human cornea," *J. Biomech.* **30**(5), 497–503 (1997).
7. R. Q. Erkamp, P. Wiggins, A. R. Skovoroda, E. Y. Emelianov, and M. O'Donnell, "Measuring the elastic modulus of small tissue samples," *Ultrason. Imaging* **20**, 17–28 (1998).
8. K. W. Hollman, E. Y. Emelianov, J. H. Neiss, G. P. Djotyan, G. Spooner, T. Juhasz, R. M. Kurtz, and M. O'Donnell, "Strain imaging of corneal tissue with an ultrasound elasticity microscope," *Cornea* **21**(1), 68–73 (2002).
9. A. R. Skovoroda, E. Y. Emelianov, and M. O'Donnell, "Reconstruction of tissue elasticity based on ultrasound displacement and strain images," *IEEE Trans. Ultrason. Ferroelectr. Freq. Control* **42**, 747–765 (1995).
10. M. R. Bryant and P. J. McDonnell, "Constitutive laws for biomechanical modeling of refractive surgery," *J. Biomech. Eng.* **118**, 473–481 (1996).
11. K. J. Parker, S. R. Huang, and R. A. Musulin, "Tissue response to mechanical vibrations for sonoelasticity imaging," *Ultrasound Med. Biol.* **16**, 241–246 (1990).
12. E. J. Chen, J. Novakofski, and W. K. Jenkins, "Young's modulus measurements of soft tissues with application to elasticity imaging," *IEEE Trans. UFFC* **43**, 191–194 (1996).
13. Y. Zeng and J. Yang, "A comparison of biomechanical properties between human and porcine cornea," *J. Biomech.* **34**(5), 533–537 (2001).
14. P. R. Greene, "Stress-strain behavior for curved exponential strips," *Bull. Math. Biol.* **47**(6), 757–764 (1985).
15. T. Juhasz, R. M. Kurtz, C. Horvath, C. Suarez, F. Raksi, Z. Bor, and G. Spooner, "The femtosecond blade: new developments in corneal refractive surgery," *Opt. Photonics News* pp. 24–29 (2002).
16. R. M. Kurtz, G. J. R. Spooner, K. R. Sletten, K. G. Yen, S. I. Sayegh, F. H. Loesel, C. Horvath, H. L. V. Elnor, D. Cabrera Fernández, M.-H. Muenier, Z. S. Sacks, and T. Juhasz, "Femtosecond laser corneal refractive surgery," *Proc. SPIE* **3591**, 209–219 (1999).
17. I. Ratkay-Traub, T. Juhasz, and C. Horvath, "Ultra-short (femtosecond) laser surgery: initial use in LASIK flap creation," *Ophthalmol. Clinics North Am.* **14**, 347–355 (2001).
18. P. R. Greene, "Mechanical considerations in myopia," *Am. J. Optom. Physiol. Opt.* **57**, 902–914 (1980).
19. H. L. Sang, *MSC/Nastran, Handbook for Nonlinear Analysis*, Version 67, The Macneal-Schwendler Corporation, Los Angeles, CA (1992).
20. K. J. Bathe, *Finite Element Procedures in Engineering Analysis*, Prentice Hall, New York (1996).
21. *Nonlinear Finite Element Structural Analysis*, Training Manual COSMOS/M, Version 1.7, Mar. 1994.
22. J. I. Barraquer, "Basis of refractive keratoplasty," *Refract. Corneal Surg.* **5**, 179–193 (1967).
23. D. T. Azar and S. G. Farah, "Laser in situ keratomileusis versus photorefractive keratectomy: an update on indications and safety," *Ophthalmology* **105**(8), 1357–1358 (1998).
24. *MATLAB Software Package*, v. 5.1, The MathWorks, Inc., Natick, MA (1997).
25. M. R. Bryant, V. Marchi, and T. Juhasz, "Predictability of picosecond laser keratomileusis for high miopia," *J. Refract. Surg.* **16**(2), 155–162 (2000).
26. D. M. Maurice, "The biology of wound healing in the corneal stroma," *Cornea* **6**(3), 162–168 (1987).
27. *Nonlinear Finite Element Structural Analysis*, Training Manual COSMOS/M, Version 1.7, Mar. 1994.
28. Y. Komai and T. Ushiki, "The three-dimensional organization of collagen fibrils in the human cornea and sclera," *Invest. Ophthalmol. Visual Sci.* **32**, 2244–2258 (1991).
29. B. E. McCarey, P. C. Baker, and R. P. Vito, "Holographic analysis of corneal biomechanics," *Invest. Ophthalmol. Visual Sci.* **33**, 896 (1992).
30. D. Cabrera Fernández, "Computational and analytical modeling of eye refractive surgery," *ProQuest Digital Dissertation*, (ISBN: 0-493-73300-0) (2002).
31. D. Cabrera Fernández, A. S. Niaz, G. P. Djotyan, R. M. Kurtz, and T. Juhasz, "Computational modeling of corneal refractive surgery," *Proc. SPIE* **5314**, 59–70 (2004).